This paper describes objective technical results and analysis. Any subjective views or opinions that might be expressed in the paper do not necessarily represent the views of the U.S. Department of Energy or the United States Government.

Sub Topic: Fire

SAND2019-10567C

Fall Technical Meeting of the
Western States Section of the Combustion Institute
October 14–15, 2019
Albuquerque, New Mexico

Predicting Limits of Cascading Failure of Thermal Runaway in Stacks of Li-Ion Pouch Cells

Andrew J. Kurzawski[1,*], *Randy Shurtz*[1], *Loraine Torres-Castro*[2], *Joshua Lamb*[2], *and John C. Hewson*[1]

[1]*Fire Science and Technology, Sandia National Laboratories, Albuquerque, NM 87185-1135, United States*

[2]*Power Sources R&D, Sandia National Laboratories, Albuquerque, NM 87185-1135, United States*

[*]*Corresponding author:* akurzaw@sandia.gov

Abstract: If a lithium-ion cell in a large-scale energy storage system goes into thermal runaway, there is a possibility that thermal runaway will cascade through the system. While losses and heat release associated with single cells are modest, cascading failure is much more severe. An understanding of the heat losses and heat transfer pathways from a cell or stack of cells undergoing thermal runaway is important to informing mitigation strategies. Identification of the most sensitive parameters involved in these predictions can aid in defining limits of propagating failure. We examine these parameters in the context of experimental measurements and finite element modeling of stacks of pouch cells with and without passive mitigation.

Keywords: ***Thermal Runaway, Lithium-ion Batteries, Mitigation***

1. Introduction

Lithium-ion batteries have energy densities that are typically in the range of 300 to 800 kJ/kg with specific heats of approximately 0.8 $kJ/kg/K$, which means that discharging the stored energy can raise the cell temperature between 400 and 1000 K. In addition, these cells are constructed with highly reactive active materials, a lithium-intercalated graphite forms the anode that represents the "fuel" while an over-oxidized metal oxide cathode plays the role of the "oxidizer."[1] These materials are separated in the cell by an electrolyte which nominally would be unreactive with either at normal operating temperatures. However, the high energy densities of the cell are tied to high reactivities of both the anode and cathode. Efforts to minimize the reactivity with the electrolyte have led to the selection of alkyl-carbonate-based solvents with lithium hexafluorophosphate salts as the most common electrolyte. Under normal operation the electrolyte reacts minimally with the cathode but reacts to form a passivation layer on the anode referred to as the solid-electrolyte inter-phase (SEI) [2–6].

If batteries are subject to abusive conditions where temperatures exceed normal operation, a sequence of reactions are observed to occur. First, there is a chemical breakdown of the SEI layer that is mildly exothermic around 100^oC. This is followed by reactions where the anode reduces the electrolyte [5–8] and at slightly higher temperatures (around 150^oC to 250^oC under ignition conditions) the cathode begins to oxidize the electrolyte [9–11]. Both of these latter reactions

Sandia National Laboratories is a multimission laboratory managed and operated by National Technology & Engineering Solutions of Sandia, LLC, a wholly owned subsidiary of Honeywell International Inc., for the U.S. Department of Energy's National Nuclear Security Administration under contract DE-NA0003525.

are significantly exothermic and can lead to violent heat release. This heat release also causes a fraction of the electrolyte to be vented into the surrounding air where it is capable of flaming combustion [12].

For larger scale installations, energy storage is generally provided by stacking large numbers of smaller cells together. There is the possibility that a localized failure or external abuse condition will lead to thermal runaway of one of the cells. The heat release associated with single cells might be 50 to 500 *kJ* but the energy of the complete installation could be one thousand times greater, and a significant question is the extent to which a single point failure will propagate to the rest of the system. This is referred to as cascading failure.

Cascading failure is related to premixed flame propagation since the internal structure can often be treated as a homogenized mixture, but there are several complexities. First, there is no reactant diffusion so that analyses associated with thermal-diffusive instabilities need to be applied. Second, the propagation through cells is often unsteady due to the interference of gaps between cells. This work addresses the prediction of cascading failure propagation through a stack of lithium-ion cells.

In this work, we compare a finite element model with experimental measurements for thermal runaway in a system consisting of 3 AH $LiCO_2$-graphite pouch cells arranged in a stack of 5 cells [13]; several different thermal configurations are considered as discussed in the results. These simulations were conducted using the SIERRA/Aria finite element software package [14]. In addition to comparing to thermocouple (TC) measurements, we use the model to examine the implications of choices of the specific model forms used in this implementation.

2. Experimental overview

The system studied in this work consists of 5 pouch cells with and without metal spacer plates placed between each cell. Thermocouples were used to measure skin temperatures of the cells at the locations depicted in Figure 1. Additionally, the voltage was measured at each cell. The dimensions of each cell were 13 *cm* by 3.55 *cm* by 0.74 *cm*.

In each test, thermal runaway was initiated by penetrating cell 1 with a 3 *mm* diameter steel nail. For the cases without plates, the initial state of charge (SOC) was varied between 50% and 100%. In the spacer plate cases, the SOC was 100% and copper or aluminum plates with thicknesses of 1/8", 1/16", or 1/32" were inserted between each of the cells (see Fig. 1). The stack of cells was constrained by a metal assembly with phenolic end blocks placed between the assembly and cells 1 and 5.

3. Finite element model

The finite element model used in this study was the SIERRA multimechanics module: Aria [14]. We approximate the stack of phenolic end blocks, cells, and spacers with a thin domain of hexahedron elements as conductivity in the plane of the electrodes is large relative to conductivity between electrode layers. The result is a quasi-1-D model of the system where the domain is discretized through the stack. In this direction, the spatial discretization is 0.1 *mm* in the cells, 0.2 *mm* in the spacers, and 0.4 *mm* in the end blocks with the domain dimensions tangent to the plane of the electrodes being 0.2 *mm* each.

Several notable assumptions were made in addition to the quasi 1-D approach. Bulk thermal properties are used for the cells, spacer plates, and end blocks, and the metal holder assembly is not

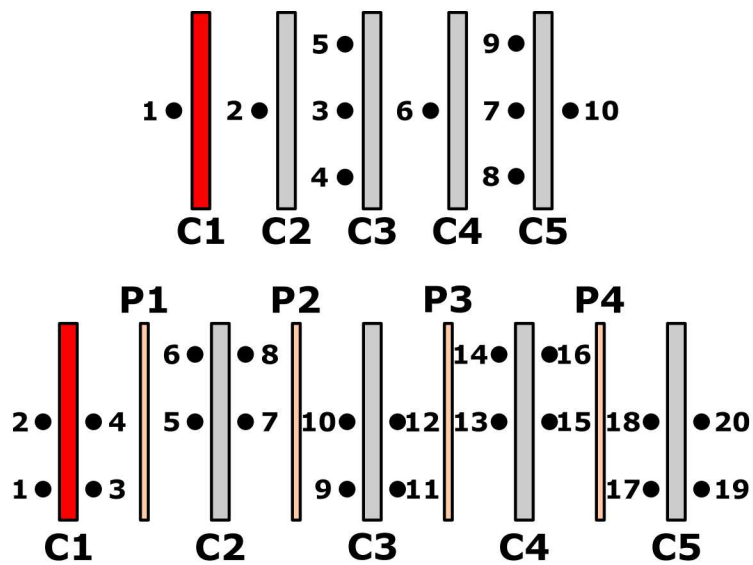

Figure 1: Expanded side view of the experimental system of cells ('C#') and plates ('P#') where thermocouple locations are depicted by numbered dots for the no-plate arrangement (top) and spacer plate arrangement (bottom).

modeled as the end blocks are assumed to provide adequate insulation. Species transport between elements and venting of electrolyte are not modeled. Heat losses to the surroundings are assumed to be convective only with a heat transfer coefficient of 5 $W/m^2/K$.

3.1 Conservation equations

The model solves the energy and species conservation equations for temperature (T) and species concentration (ρ_i).

$$\rho c_p \frac{\partial T}{\partial t} = \nabla \cdot (K \nabla T) + \dot{q}''' \tag{1}$$

The following thermal properties are defined for each material in the system: density (ρ), specific heat (c_p), and thermal conductivity (K). The volumetric heat source term depends on the reaction rates (r_j) and energy release (ΔH) for each of the N_r reactions.

$$\dot{q}''' = \sum_{j=1}^{N_r} \Delta H_j r_j \tag{2}$$

The species conservation equation is given by

$$\frac{\partial \rho_i}{\partial t} = \sum_{j=1}^{N_r} (\nu''_{ij} - \nu'_{ij}) r_j \tag{3}$$

where species are indexed by subscript i, reactions are indexed by subscript j, and ν''_{ij} is the stoichiometric coefficient of species i being produced in reaction j and ν'_{ij} is the stoichiometric coefficient of species i being consumed in reaction j.

Convective boundary conditions are applied to the surface of the stack, and the heat transfer coefficient (h) is adjusted for the change in volume (V) and area (V) from the full domain (subscript 1) to the quasi-1-D domain (subscript 2).

$$h_2 = h_1 \frac{A_1}{A_2} \frac{V_2}{V_1} \tag{4}$$

3.2 Reaction models

In this work, we model thermal runaway in these specific cells with four global reactions that represent distinct processes: a nail short circuit, decomposition of the solid electrolyte inter-phase (SEI), the anode critical thickness model, and a single step cathode model. These reactions are typically modeled with Arrhenius forms where the model constants are calibrated by comparison to calorimetry measurements such as differential scanning calorimetry (DSC) and accelerating rate calorimetry (ARC). These measurement techniques succeed in capturing the onset of thermal runaway, but may have difficulty keeping up with the rapid heat release after onset depending on the size of the sample and configuration of the calorimeter. The calorimetry data is typically only accurate within the range from ambient temperature to 250^oC. Cells undergoing thermal runaway experience heat release occurring up through significantly higher temperatures, and more heat release data is needed from 300 to 1000^oC. Here we present the models from literature that are used in the current finite element model reserving discussion of the adjustments to the model constants for Section 4.

Within a cell, lithium intercalated in graphite, C_6Li, represents a fuel that reacts electrochemically with an over-oxidized metal oxide like CoO_2. The products of this reaction are $LiCoO_2$ and C_6. During thermal runaway, an internal short circuit reaction can allow this reaction to proceed, releasing the chemical energy internally. The short circuit reaction resulting from nail penetration is only applied over a 2 *mm* wide section of cell 1. The reaction is represented as

$$\mathrm{C_6Li} + \mathrm{CoO_2} \rightarrow \mathrm{LiCoO_2} + \mathrm{C_6} \tag{5}$$

to capture lithium transport from the anode to cathode. The reaction rate is constructed to approximate the relationship between voltage and state of charge as follows

$$r_1 = A_1 \rho_{C_6Li}^{0.1} \tag{6}$$

where the constant A_1 is inversely proportional to a short resistance parameter that was adjusted to match the onset of heating observed by thermocouples adjacent to cell 1.

The SEI decomposition reaction proposed by Richard and Dahn is given as [7, 8]

$$r_2 = \rho_{SEI}^{0.5} A_2 exp(-E_2/RT) \tag{7}$$

where the SEI is assumed to be converted to a Li_2CO_3 salt and a lumped gas.

At high temperatures, the lithium anode reacts with the electrolyte, represented here as ethylene carbonate, $C_3H_4O_3$. An update to the work of Richard and Dahn from Shurtz, et al. [5, 6] for the reaction of the lithiated graphite anode and electrolyte is given as

$$\mathrm{2C_6Li} + \mathrm{C_3H_4O_3} \rightarrow \mathrm{2C_6} + \mathrm{Li_2CO_3} + \mathrm{Gas} \tag{8}$$

where the electrolyte is abbreviated EC in future equations and additional Li_2CO_3 and gas are produced. The reaction rate is given as

$$r_3 = \rho_{C_6Li} \frac{\rho_{EC}}{\rho_{EC} + \rho_{50}} \frac{a_e}{a_o} A_3 exp(-E_3/RT) exp(-z_t) \tag{9}$$

where

$$\frac{dz_t}{dt} = -\frac{dx_i}{dt} \frac{C_t}{(a_{BET}/a_0)^{n_t}} \tag{10}$$

for $z_t < z_{crit}$ and $\frac{dz_t}{dt}$ is equal to zero otherwise and x_i is the moles of intercalated lithium normalized by moles of graphite. The edge and BET areas (a_e and a_{BET}) are material dependent and the reader is directed to [5, 6] for details on the model parameters ρ_{50}, C_t, n_t, and a_0.

Also at high temperatures the cathode oxidizes the electrolyte. We approximate the cathode reaction with a single step based on Hatchard, et al. [15]

$$\mathrm{CoO_2} + \frac{2}{15}\mathrm{C_3H_4O_3} \rightarrow \frac{1}{3}\mathrm{Co_3O_4} + \mathrm{Gas} \tag{11}$$

where the Co_3O_4 is assumed to be inert and any gaseous products are lumped in with gases produced from other steps. The reaction rate is an autocatalytic form

$$r_4 = \rho_{Co_3O_4} \rho_{CoO_2} A_4 exp(-E_4/RT) \tag{12}$$

where the heat of reaction is significantly increased from Hatchard, et al. to match the experimentally measured peak temperatures in the five cell system.

Table 1 summarizes the major reaction model parameters, and the reader is directed to the respective sources for additional parameters and model details. We note that the constant A is given in $1/s$ and appropriate unit conversions are required depending on the concentration function to give the reaction rates (r_j) in terms of the density of reactants per second. Additionally, all heats of reaction (ΔH_j) are listed in energy per mass of total reactants.

Table 1: Reaction rate model parameters.

Reaction	A	E	ΔH
	$1/s$	kJ/mol	kJ/kg
1	0.417	N/A	-2384.3
2	1.667e15	135.0	-635.0
3	2.1e13	135.0	-2287.1
4	6.667e11	122.52	-1469.3

3.3 Material properties

Thermal properties for the cells, spacer plates, and end blocks are listed in Table 2. Thermal properties for the spacer plates are from Incropera [16], and the end blocks are taken from [17].

The cells are approximated with bulk thermal properties, where the initial mass of individual species, density, and specific heat come from a tear-down of the cells components. There is some

Table 2: Material properties for system components.

Material	Thermal Conductivity $W/m/K$	Specific Heat $J/kg/K$	Density kg/m^3
Bulk Cell	0.5	778	1816
Aluminum	237	903	2702
Copper	401	385	8933
End Block	0.36	1500	1356

uncertainty associated with the amount of SEI, electrolyte, and inert components (i.e. casing, separator material, etc.). The anode and cathode masses are 8.57 g and 21.43 g respectively per cell, and we estimate each cell initially contains 3.77 g of electrolyte. The remaining inert materials make up 28.24 g.

There is significant uncertainty in the estimation of a bulk thermal conductivity perpendicular to the plane of the electrodes. Hatchard, et al. [15] estimates this value to be 3.4 $W/m/K$ for cylindrical cells, while Vishwakarma, et al [18] estimate a value of 0.24 $W/m/K$ for a $LiCoO_2$ cathode half-cell. For this work, we have found 0.5 $W/m/K$ to be an acceptable starting value, but due to the sensitivity of the speed of the reaction front to thermal conductivity, a more detailed analysis should be done in the future.

Thermal contact resistance is expected to play a major role in cell to cell propagation of thermal runaway. A higher thermal contact resistance will delay the onset of thermal runaway in cells adjacent to a failed cell, however swelling of the cell container pouch can increase pressure between cells thereby decreasing thermal contact resistance. For this work, a contact resistance of 2e-3 m^2K/W was found to adequately capture the cell-to-cell propagation times.

4. Comparison of experiments and model results

We begin with a comparison of the quasi 1-D finite element model and experimental results for the no-spacer case at 100% SOC (referred to as the base case). This simulation uses the original reaction rates determined from low-temperature (below 250^oC) measurements as noted above. The simulated and experimental thermocouple temperatures are shown in Figure 2. The speed of the reaction front through the stack is greatly over-predicted as the simulated cell stack finishes thermal runaway in $\sim$20 seconds while the experimental cells take $\sim$100 seconds for the propagation front to reach thermocouple (TC) 10.

The thermal runaway propagation front crosses each cell in approximately 10 seconds in the experiment and 1 second in the simulation presented in Figure 2. With literature reaction-rate constants calibrated using data for the onset of thermal runaway (around 150 to 200^oC) whereas the peak temperatures measured by the thermocouples are between 600 and 700^oC, the high temperature rates are highly uncertain. We wish to preserve the onset behavior while limiting the high temperature rates.

Reactions 3 and 4 (anode and cathode) are the primary contributors to fast chemistry in the cells due to the Arrhenius form and higher heat-release rate than the SEI decomposition reaction. To preserve the onset behavior, we must adjust the pre-exponential factor (A) and activation energy (E) together. Fixing the rate constant (k) at the onset temperature (T_{on}) gives

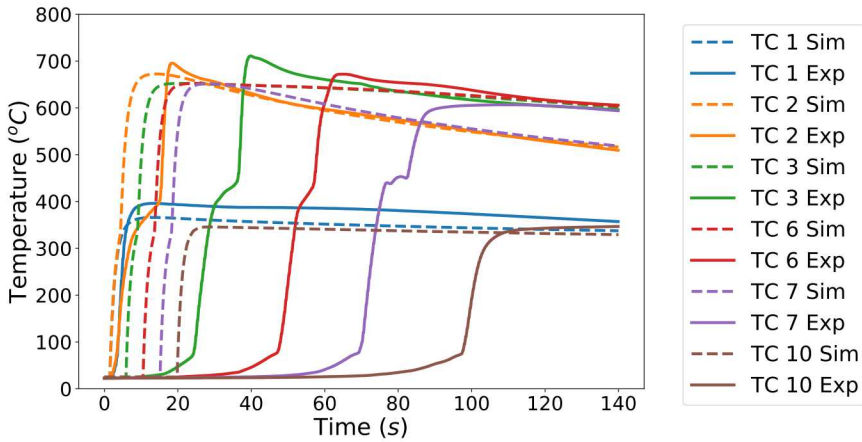

Figure 2: Baseline 100% SOC no spacer case where dashed lines are simulated thermocouples and solid lines are experimental measurements.

$$A' exp(-E'/RT_{on}) = A exp(-E/RT_{on}) \tag{13}$$

where A' and E' are the scaled pre-exponential factor and activation energy, respectively. From laminar premixed flame theory, the burning velocity scales as

$$v \propto \sqrt{\alpha k} \tag{14}$$

where α is the thermal diffusivity and k is the reaction rate constant. At the peak temperature (T_{peak}), we wish to reduce the velocity from v to v' by a factor ϕ

$$v' = \phi v \tag{15}$$

substituting the expression for burning velocity and simplifying we get

$$k'(T_{peak}) = \phi^2 k(T_{peak}) \tag{16}$$

followed by substituting the Arrhenius expression for k to arrive at

$$A' exp(-E'/RT_{peak}) = \phi^2 A exp(-E/RT_{peak}) \tag{17}$$

Given T_{on} and T_{peak}, we solve Equations 13 and 17 for A' and E' with the desired ϕ scaling. Using the Arrhenius plot in Figure 3, this is equivalent to adjusting the slope and intercept of the line about a point fixed at $1/T$ and $ln(k)$ for the onset temperature (taken to be 150^oC) shown here for Reaction 3 with a value of $\phi = 1/20$.

Preliminary investigations of scaling the propagation velocity for reactions 3 and 4 showed improved predictions with ϕ equal to $1/20$ and $1/40$ respectively (Fig. 4). The propagation velocity is still over-predicted with a time to completion of thermal runaway of $\sim$80 seconds in the simulation compared to $\sim$100 seconds in the experiment. The predicted peak temperatures of the internal thermocouples (TC 2 - TC 7) lie between 600^oC and 700^oC while the peak experimental temperatures are seen to decrease from thermocouple 3 to 7, indicating either experimental variability or the presence of physics not captured in the quasi 1-D model approximation.

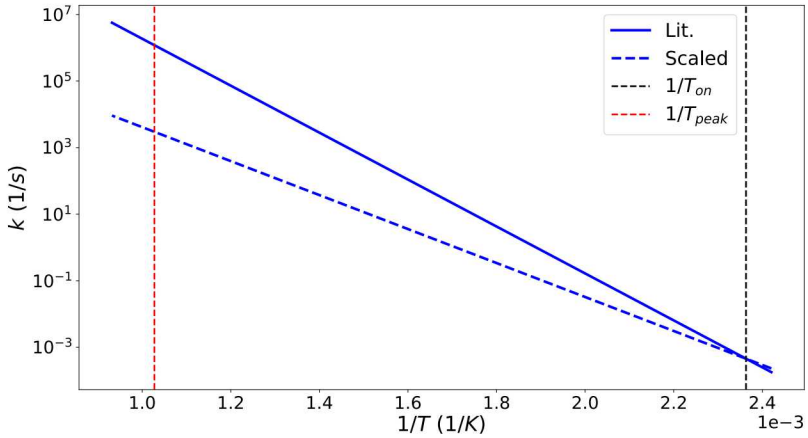

Figure 3: Example Arrhenius plot of the anode with $\phi = 1/20$.

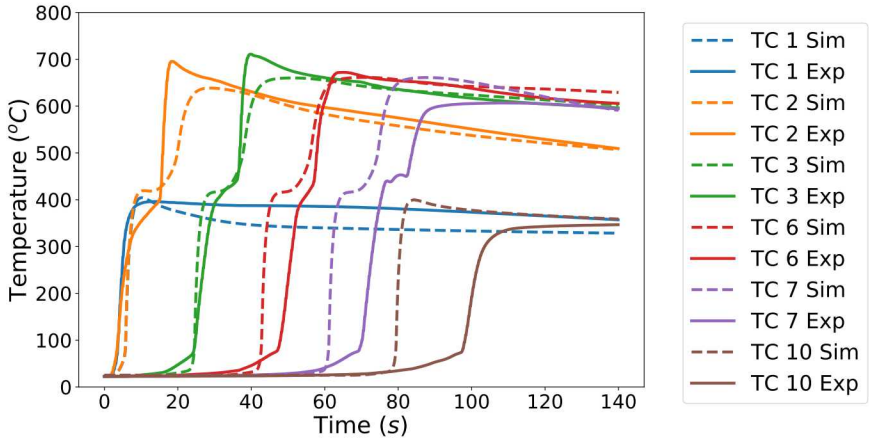

Figure 4: Baseline 100% SOC no spacer case with velocity scaling where dashed lines are simulated thermocouples and solid lines are experimental measurements.

The temperature profiles for the internal thermocouples (TC 2 - TC 7) exhibit four distinct heating regions followed by a slower cooling region. The first slow increase in temperature is due to conduction ahead of the propagation front. The next heating region is marked by a rapid increase in temperature to around 400^oC which signifies the arrival of the propagation front (i.e. the propagation front reaching the end of the battery to the left of the TC in Figure 1). Then the heating rate slows as heat from a failed cell is transferred across the gap containing the TC into the next cell in the stack. The duration of this region is primarily determined by the thermal contact resistance between cells and the amount of thermal energy that is needed to heat the next cell to thermal runaway. The final rapid increase in temperature signifies the next cell in the stack entering thermal runaway.

The heating rate at the onset of thermal runaway is also under-predicted (the second temperature rise in the internal TCs, e.x. TC 3 around 35 seconds). This could be an unintended consequence of the reaction rate scaling used here where rates at intermediate temperatures (between onset and peak temperature) may be depressed. Conversely, the heating rate when the propagation

front reached the end of a cell is over-predicted. This behavior can be seen in greater detail by examining the temperature profile in cell 2 at several points in time during thermal runaway as seen in Figure 5.

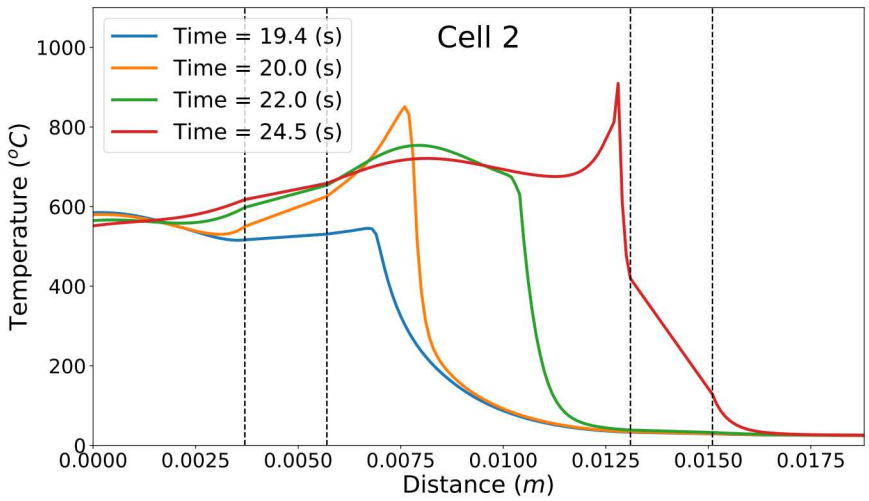

Figure 5: Temperature at several times in cell 2 of the baseline 100% SOC no spacer case. Vertical dashed lines represent the modeled contact resistance region between cells.

The onset of thermal runaway can be seen at 19.4 seconds and 20 seconds where a peak in the heating rate occurs inside the cell about 2 *mm* from the boundary with cell 1. Some of the heat from this delayed peak travels back towards cell one which can be seen in the slow temperature rise in TC 2 between 450 and 650^oC in Figure 4. Propagation of thermal runaway progresses steadily through the cell as exemplified by the temperature at 22 seconds. When the propagation front approaches the right edge of cell 2, another rapid heating event occurs due to the contact resistance slowing down heat transfer away from the reaction front and to cell 3. Based on this observation, an improvement to the relative magnitude of the contact resistance and thermal conductivity of the cells may improve this behavior.

With the improvements in propagation velocity, we can examine a variety of other scenarios for which experimental data is available. The state of charge is an indication of the energy stored in the system; partially discharged batteries have depleted the reactants. Beginning with the state of charge (SOC), experiments were run at 100%, 80%, 75%, and 50% SOC. Thermal runaway only propagated through all five cells in the 100% and 80% cases. Figure 6 shows the model predictions for the 80% SOC case compared to experimental measurements. It can be seen that in the simulation, the nail short circuit reaction does not provide enough energy to trigger thermal runaway in the remaining reactions and propagation does not occur. In the experiments, propagation occurs, but the time for the propagation front to reach the end of cell five is approximately twice as long as the 100% SOC case. Additionally, peak temperatures measured by the thermocouples are $\sim$100^oC lower than the 100% SOC case as there is less energy available to drive the reactions.

The current simulations fail to propagate below 95% SOC, while experimental results show that propagation is possible down to 80% SOC with the 75% SOC case failing to propagate. In other words, the simulation is more sensitive to variations in the stored energy than the measurements suggest. Due to the large uncertainty in many of the model parameters, there are several

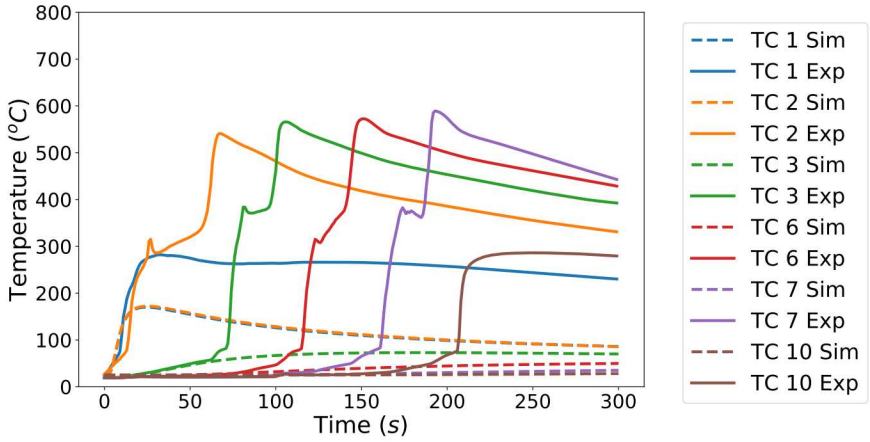

Figure 6: 80% SOC no spacer case where dashed lines are simulated thermocouples and solid lines are experimental measurements.

possible causes of this discrepancy. One potential source of this error is the heat of reaction for the cathode reaction (reaction 4). This value was estimated to combine the heat release from what is traditionally represented as a two step reaction, and further detailed analysis should be conducted to determine an appropriate value for the single step approximation. The velocity limiter may be introducing a source of error in the intermediate temperature ranges between the initiation temperature and maximum temperatures. While the limiter effectively regulates the propagation velocity at the maximum temperature, it may be inhibiting propagation from proceeding in intermediate temperature regions.

Experiments were conducted with copper and aluminum spacer plates with thicknesses of 1/32", 1/16", and 1/18". These spacer plates also provide another means of 'diluting' the reactants, here with additional thermal mass in between cells. Propagation through the entire stack of cells was only observed with the 1/32" spacer cases. Figure 7 shows the comparison of simulated and experimental temperature for the 1/32" aluminum spacer case. We note that the thermocouples have been relabeled with respect to Figure 1 for ease of identifying the location of each thermocouple with respect to the cells and plates. The legend describes the adjacent cell number as 'T Cell #', and the location in the plane of the electrodes is signified by 'M' for the middle of the cell. The final value in the legend key is either 'O' for the outside of the cell next to an end block, or 'P#' for the adjacent plate number. For example 'T Cell 2 (M-P2)' corresponds to TC 7 from Figure 1 (bottom) as it is the thermocouple located between to cell 2 and plate 2.

Similar to the 100% SOC base case, the simulated propagation velocity is slightly faster than the observed experimental velocity for the 1/32" aluminum spacer case. We note that the TC between cell 3 and plate 3 failed during the experiment. The trends in the peak temperatures are also similar to the base case with a tendency towards under-prediction in the first four cells and over-prediction around the last cell. During the lag time between cells 1 and 2 undergoing thermal runaway, the thermocouples on either side of plate 1 measure a greater difference in temperature compared to the simulation (TCs 1 M-P1 and 2 M-P1). This could be a result of the estimated contact resistance between the spacer and cell casing being too low.

However, in the 1/32" copper spacer case, the simulation fails to predict propagation while full propagation is observed in the experiment as seen in Figure 8. The peak temperature in cell 1 and

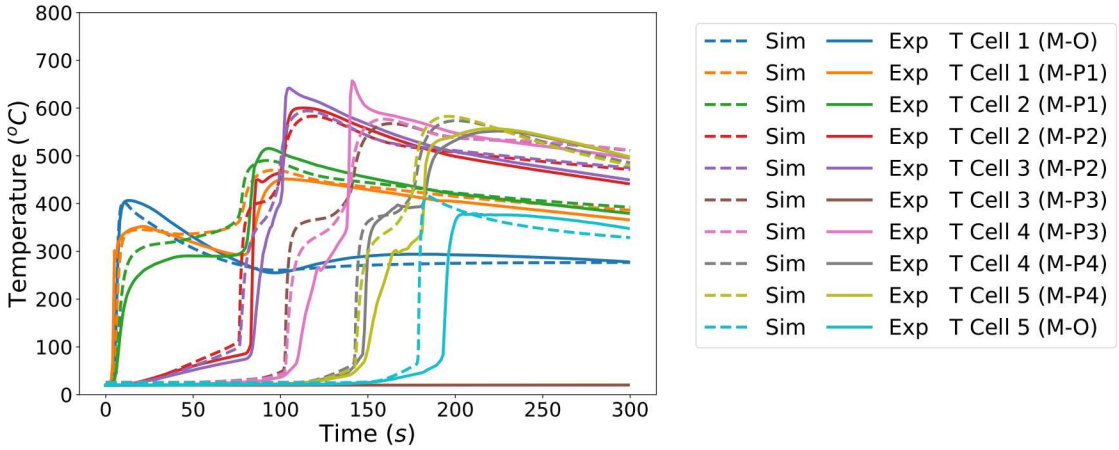

Figure 7: 100% SOC with 1/32" aluminum spacer plates where dashed lines are simulated thermocouples and solid lines are experimental measurements.

subsequent temperature rise in cell 2 are predicted well, but initiation of thermal runaway does not occur.

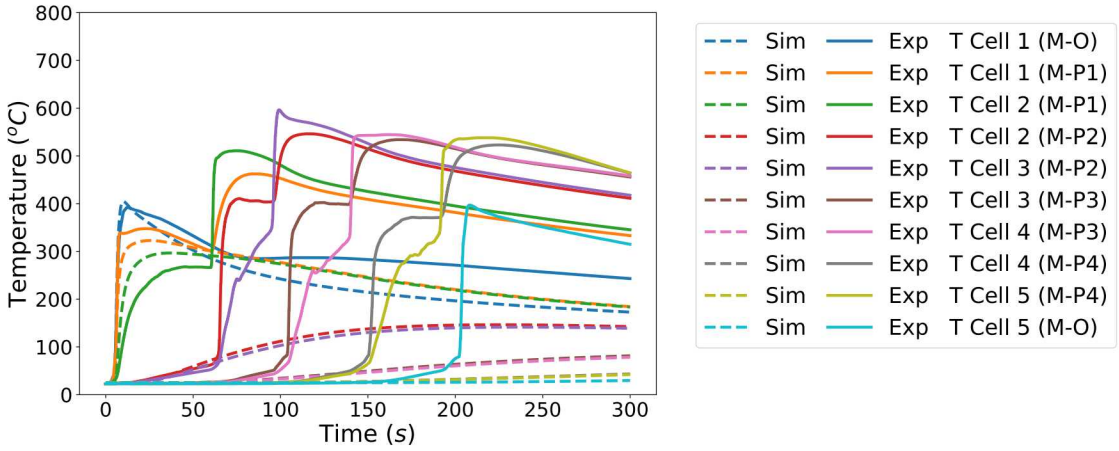

Figure 8: 100% SOC with 1/32" copper spacer plates where dashed lines are simulated thermocouples and solid lines are experimental measurements.

For both 1/16" spacer materials, full propagation did not occur in both the experiments and simulations. The 1/16" copper spacer case is shown in Figure 9. Similar to the 1/32" case, the thermocouples around plate 1 measure a larger gap than what is predicted. Contrary to the observations from the base case, predictions of conductive heat transfer ahead of the cell undergoing thermal runaway closely follow the experiments as seen in TCs 2 (M-P2) and 3 (M-P2).

To diagnose the difference between the predictions of propagation in the 1/32" aluminum spacer case and no propagation in the 1/32" copper spacer case, we examine the simulated temperature profiles at the beginning of thermal runaway in cell 2 (Fig. 10). At a time of 51.5 seconds, both reactions 3 and 4 are active at the left edge of cell 2, but the copper case will not reach the higher rates and the heat will be dissipated while the aluminum case will continue propagating.

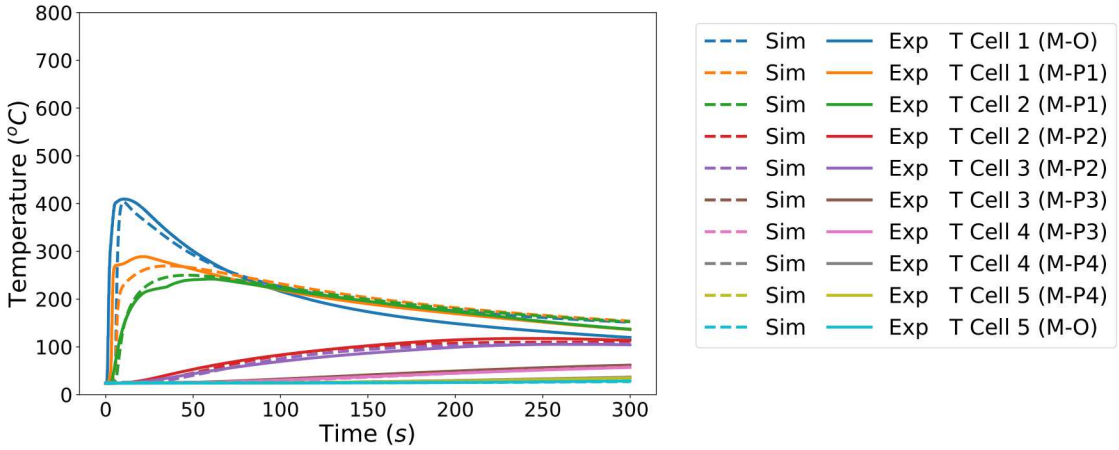

Figure 9: 100% SOC with 1/16" copper spacer plates where dashed lines are simulated thermocouples and solid lines are experimental measurements.

Based on observations from the literature [15], temperatures over 150^oC should be sufficient to trigger thermal runaway. In the simulation, cell 2 in the copper case is reaching 300 ^oC and not progressing to thermal runaway. This adds evidence to the hypothesis that the velocity limiter is having an adverse effect on predictions at intermediate temperatures by decreasing the reaction rate. A different model form that captures onset, intermediate temperature, and high temperature behavior should be explored in the future.

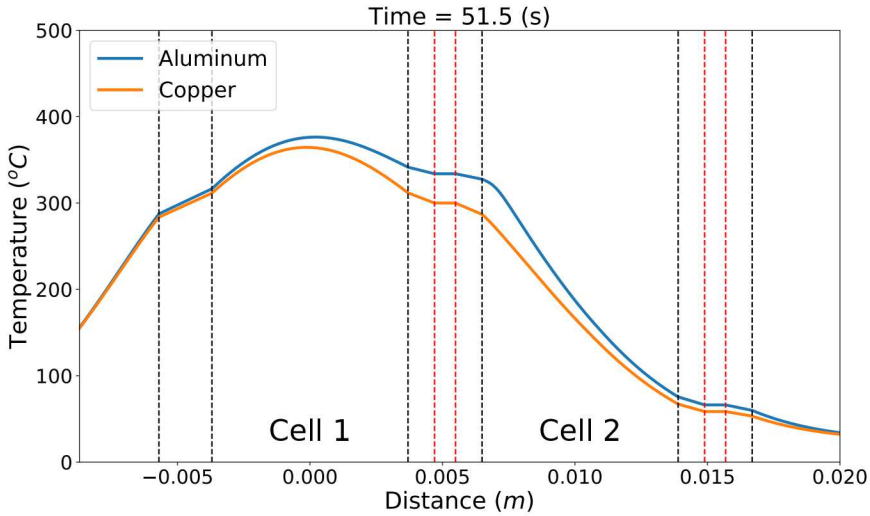

Figure 10: Temperature at the onset of thermal runaway in cell 2 for the 1/32" spacer cases. Black vertical dashed lines represent the modeled contact resistance region between cells, and red lines are the spacer boundaries.

5. Conclusions

In this work, we examined finite element model predictions of propagation of thermal runaway through a stack of pouch cells compared to experimental temperature measurements. These predictions were made with a set of nominal parameters describing the material properties and reaction model constants. Adjustments were made to slow the propagation speed at the peak temperature. This improved predictions in the 100% SOC case, but the limits of propagation were more sensitive to reduced energy content and more sensitive to thermal masses placed between cells than observed in the experiments. Additional insights were drawn from the model behavior with respect to the experimental measurements that will be beneficial for improving model parameters and model forms in future studies. Most notable among these insights were the effects of reaction-rate damping at intermediate temperatures and the effect of the interplay between thermal conductivity and contact resistance on inhomogeneous thermal energy transfer near the cell boundaries.

6. Acknowledgements

The authors gratefully acknowledge funding from the Department of Energy, Office of Electricity's Energy Storage Program, under the direction of Dr. Imre Gyuk. Sandia National Laboratories is a multi-mission laboratory managed and operated by National Technology and Engineering Solutions of Sandia, LLC., a wholly owned subsidiary of Honeywell International, Inc., for the U.S. Department of Energy's National Nuclear Security Administration under contract DE-NA0003525. This paper describes objective technical results and analysis. Any subjective views or opinions that might be expressed in the paper do not necessarily represent the views of the U.S. Department of Energy or the United States Government.

SAND No. SAND2019-XXXX

References

[1] B. Scrosati and J. Garche, Lithium batteries: Status, prospects and future, J. Power Sources 195 (2010) 2419–2430.

[2] E. Peled, The electrochemical behavior or alkali and alkaline-earth metals in non-aqueous battery systems – the solid electrolyte interphase model, J. Electrochem. Soc. 126 (1979) 2047–2051, URL: %3CGo%20to%20ISI%3E://A1979JM04200001.

[3] D. Aurbach, Review of selected electrode-solution interactions which determine the performance of Li and Li ion batteries, J. Power Sources 89 (2000) 206–218, URL: %3CGo%20to%20ISI%3E://000087938100014.

[4] D. Aurbach, Y. Gofer, M. Benzion, and P. Aped, The behavior of lithium electrodes in propylene and ethylene carbonate – the major factors that influence Li cycling efficiency, Journal of Electroanalytical Chemistry 339 (1992) 451–471.

[5] R. C. Shurtz, J. D. Engerer, and J. C. Hewson, Predicting High-Temperature Decomposition of Lithiated Graphite: Part I. Review of Phenomena and a Comprehensive Model, Journal of The Electrochemical Society 165 (2018) A3878–A3890.

[6] R. C. Shurtz, J. D. Engerer, and J. C. Hewson, Predicting High-Temperature Decomposition of Lithiated Graphite: Part II. Passivation Layer Evolution and the Role of Surface Area, Journal of The Electrochemical Society 165 (2018) A3891–A3902.

[7] M. Richard and J. Dahn, Accelerating rate calorimetry study on the thermal stability of lithium intercalated graphite in electrolyte. I. Experimental, Journal of The Electrochemical Society 146 (1999) 2068–2077.

[8] M. Richard and J. Dahn, Accelerating rate calorimetry study on the thermal stability of lithium intercalated graphite in electrolyte. II. Modeling the results and predicting differential scanning calorimeter curves, Journal of The Electrochemical Society 146 (1999) 2078–2084.

[9] L. Ma, M. Y. Nie, J. Xia, and J. R. Dahn, A systematic study on the reactivity of different grades of charged Li NixMnyCoz O-2 with electrolyte at elevated temperatures using accelerating rate calorimetry, Journal of Power Sources 327 (2016) 145–150.

[10] D. D. MacNeil and J. R. Dahn, The reaction of charged cathodes with nonaqueous solvents and electrolytes - I. Li0.5CoO2, J. Electrochem. Soc. 148 (2001) A1205–A1210, URL: %3CGo%20to%20ISI%3E://000171653100001.

[11] D. D. MacNeil and J. R. Dahn, The reactions of Li0.5CoO2 with nonaqueous solvents at elevated temperatures, J. Electrochem. Soc. 149 (2002) A912–A919.

[12] P. A. Glaude, W. J. Pitz, and M. J. Thomson, Chemical kinetic modeling of dimethyl carbonate in an opposed-flow diffusion flame, Proceedings of the Combustion Institute 30 (2005) 1111–1118.

[13] L. Torres-Castro, J. Lamb, A. Kurzawski, and J. Hewson, Passive mitigation of failure propagation in multi-cell lithium ion batteries, in preparation for J. Electrochem. Soc. (2019).

[14] SIERRA Thermal/Fluid Development Team, SAND2019-3786, SIERRA Multimechanics Module: Aria User Manual – Version 4.52, Report Report No., April 2019.

[15] T. Hatchard, D. MacNeil, A. Basu, and J. Dahn, Thermal model of cylindrical and prismatic lithium-ion cells, Journal of The Electrochemical Society 148 (2001) A755–A761.

[16] F. P. Incropera, A. S. Lavine, T. L. Bergman, and D. P. DeWitt, Fundamentals of heat and mass transfer, Wiley, 2007.

[17] Tufnol Composites Ltd., *TUFNOL Grade 6F/45*, 2019, URL: https://www.tufnol.com/materials-full/fabric_laminates/tufnol-grade-6f-45.aspx (visited on 08/19/2019).

[18] V. Vishwakarma, C. Waghela, Z. Wei, R. Prasher, S. C. Nagpure, J. Li, F. Liu, C. Daniel, and A. Jain, Heat transfer enhancement in a lithium-ion cell through improved material-level thermal transport, Journal of Power Sources 300 (2015) 123–131.